ARTICLE

Hydrogenated vacancies lock dislocations in aluminium

Degang Xie[1], Suzhi Li[2], Meng Li[1], Zhangjie Wang[1], Peter Gumbsch[2,3], Jun Sun[1], Evan Ma[1,4], Ju Li[1,5] & Zhiwei Shan[1]

Due to its high diffusivity, hydrogen is often considered a weak inhibitor or even a promoter of dislocation movements in metals and alloys. By quantitative mechanical tests in an environmental transmission electron microscope, here we demonstrate that after exposing aluminium to hydrogen, mobile dislocations can lose mobility, with activating stress more than doubled. On degassing, the locked dislocations can be reactivated under cyclic loading to move in a stick-slip manner. However, relocking the dislocations thereafter requires a surprisingly long waiting time of $\sim 10^3$ s, much longer than that expected from hydrogen interstitial diffusion. Both the observed slow relocking and strong locking strength can be attributed to superabundant hydrogenated vacancies, verified by our atomistic calculations. Vacancies therefore could be a key plastic flow localization agent as well as damage agent in hydrogen environment.

[1] Center for Advancing Materials Performance from the Nanoscale (CAMP-Nano) & Hysitron Applied Research Center in China (HARCC), State Key Laboratory for Mechanical Behavior of Materials, Xi'an Jiaotong University, Xi'an 710049, China. [2] Institute for Applied Materials, Karlsruhe Institute of Technology, 76131 Karlsruhe, Germany. [3] Fraunhofer-Institut für Werkstoffmechanik IWM, 79108 Freiburg, Germany. [4] Department of Materials Science and Engineering, Johns Hopkins University, Baltimore, Maryland 21218, USA. [5] Department of Nuclear Science and Engineering and Department of Materials Science and Engineering, Massachusetts Institute of Technology, Cambridge, Massachusetts 02139, USA. Correspondence and requests for materials should be addressed to J.L. (email: liju@mit.edu) or to Z.S. (email: zwshan@mail.xjtu.edu.cn).

Hydrogen is incorporated into many industrially important metals during processing or service, and often has deleterious consequence on mechanical properties that is commonly referred to as hydrogen embrittlement (HE). Despite numerous efforts over the past century[1], the exact mechanism of hydrogen effects on the ability of the material to plastically deform remains controversial. For example, both softening and hardening effects were observed in macroscopic tensile tests[2–5]. Also, the fracture surfaces of hydrogen-embrittled materials usually contain features indicative of pronounced local plastic deformation[6–8]. Knowing exactly how hydrogen interacts with dislocations—the primary carriers of plasticity, is therefore important.

There are debates over hydrogen effects on dislocation motion. According to Cottrell's theory, diffusible atoms are expected to cause a resistance to dislocation motion by forming an atmosphere around the dislocation, that could drag it[9]. Birnbaum and Robertson et al.[10,11] proposed that by reducing the long-range elastic interaction between dislocations, hydrogen generates a 'shielding' effect that makes individual dislocation motion easier in a train of same-sign dislocations. However, their experimental set-up may not guarantee that the applied 'constant strain' or 'constant stress' was truly constant when tens of torrs of hydrogen gas flooded the TEM chamber, as fresh dislocations were seen to be generated in the 'constant strain' stage[12]. Song and Curtin[13,14] stated based on atomistic calculations that the hydrogen interstitial atmosphere dressing a dislocation provides little shielding of elastic interaction; it also reduces rather than enhances the dislocation mobility. These mechanisms are hydrogen concentration, temperature and strain-rate dependent, and are not necessarily mutually exclusive.

Hydrogen has been experimentally found to facilitate the preservation of superabundant vacancies (SAVs) in a large variety of metals and alloys[15–17]. With SAVs inside, a dislocation can meet and even pick up these tiny 'obstacles' along its gliding path[18], or attract SAVs toward it during waiting time. The behaviour of dislocations is thus expected to be modified in the presence of hydrogen-stabilized SAVs. In some measurements[16], the vacancy concentration can even exceed the hydrogen concentration. The role of SAVs in dislocation motion was however not taken into account in previous studies of hydrogen–dislocation interaction, to the best of our knowledge. The SAVs were also supposed to play a role in the fracture of metals[18–24], as a form of microscale damage (the smallest void or bubble) that reduces the total metal–metal coordination number in a sample.

Since dislocation dynamics can be influenced by both hydrogen interstitial and hydrogenated vacancy, and neither of them can be directly visualized, experimental verification of hydrogen/vacancy effect on dislocation behaviour is very challenging. To resolve this issue, we note that relative to the fast interstitial diffusion of hydrogen atoms, the diffusion of hydrogenated vacancy would be at least two orders of magnitude slower at room temperature[16,25,26]. Therefore, an effective way to differentiate the two is to measure the time scale of their trapping kinetics on individual dislocation motion through cyclic loading, with different in-between aging times, in vacuum and in hydrogen environment, respectively. We show that the segregation time for hydrogen to lock dislocation motion is at least two orders more than the prediction based on interstitial hydrogen diffusion. Thus, hydrogen-vacancy complexes are proposed to be the effective diffusing species, at odds with the widely accepted knowledge of hydrogen–dislocation interaction. These results are relevant for modelling hydrogen embrittlement.

Results

In situ **mechanical tests**. A single-crystal aluminium pillar sample with diameter of ∼620 nm is chosen because dislocations can be imaged easily and clearly inside TEM. The pillar top is covered by a deposited carbonaceous layer of ∼100 nm to buffer disturbances from rough contacts between the Al pillar and the diamond punch during multiple compression tests. As shown in Fig. 1a, the as-prepared pillar has a high density of dislocations. Therefore, we take advantage of the 'cyclic healing' phenomenon[27,28] to clean up the interior of the pillar, using the loading function shown in Fig. 1b with peak stresses of ∼330 or ∼250 MPa. The detailed healing process is in Supplementary Fig. 1 and Supplementary Note 1. Shown in Fig. 1c are samples after the cyclic healing, in which only a few mobile dislocations delineated by the white solid lines remained. It is interesting that three of the five dislocations marked in Fig. 1c exhibited sudden forward jump at a critical threshold stress. Presumably, this should arise from overcoming some pinning points along the dislocation line. The slow loading rate in the leading cycle of each cyclic test group allows us to resolve the de-pinning stress of each dislocation by mapping the stress data to the movie frames (Supplementary Fig. 2). As shown in Fig. 1d, the critical stress for these dislocation jumps decreases with increasing cycle number.
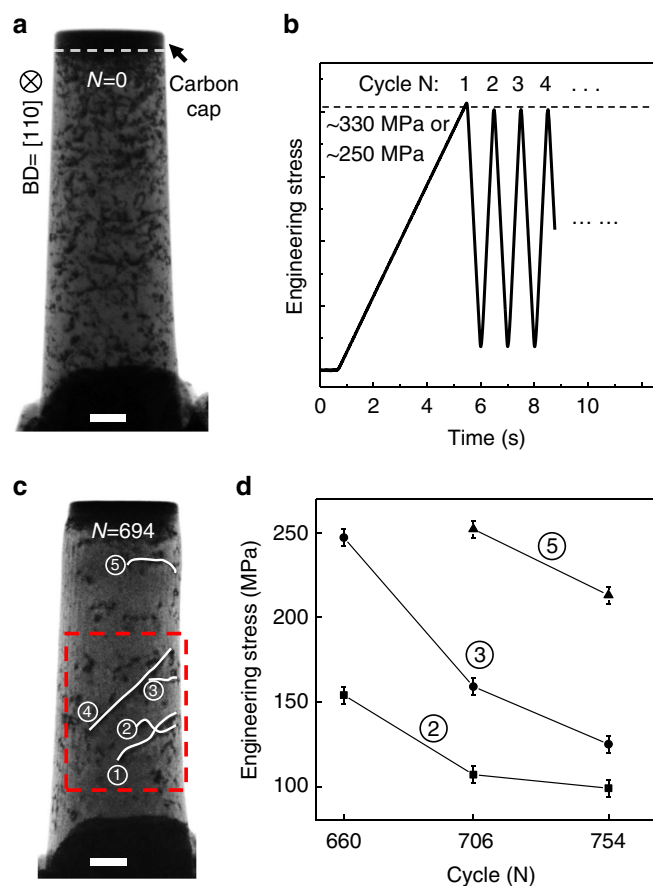

Figure 1 | Mechanical annealing and stabilization of dislocations inside the aluminium pillar. (**a**) The as-fabricated pillar shows high dislocation density, and a carbon cap is deposited atop the pillar as a buffer layer to ensure stable contact between multiple tests. (**b**) The loading curve used in cyclic compression tests. (**c**) After 694 cycles of cyclic compression, the dislocation density is dramatically decreased, leaving only 5 mobile dislocations. The region in the red dashed rectangle is examined in detail, see Figs 2–4. (**d**) The measured critical stress for dislocation forward-jump decreases with loading cycle, for each dislocation. Error bars represent standard deviation. All scale bars are 200 nm.

This indicates that the more loading cycles these dislocations have experienced, the weaker the pinning becomes. For example, from $N = 660$ to 754 (N indicates number of cycles), the critical stress for the jump of dislocation #2 dropped from $\sim$150 to $\sim$100 MPa.

Electron beam irradiation can displace aluminium atoms off its lattice sites, producing vacancies which may gather around dislocations with time. To identify aging effect on dislocation behaviour from irradiation-induced vacancies, a vacuum aging experiment, with and without the e-beam, was designed to check whether waiting for an extended period in vacuum in lieu of hydrogen exposure would affect dislocation motion (Supplementary Movie 1). Before the aging experiment, dislocations move between delineated positions (white dash lines at $\sim$27 MPa, and white solid lines at $\sim$250 MPa, Fig. 2a). Then the pillar was subjected to the aging process, which consisted of $\sim$170 min of beam-off waiting and $\sim$30 min of beam-on waiting at room temperature. After aging, the density of dislocation remained unchanged, although some individual dislocations underwent minor profile change (Fig. 2b,c). For example, curved segments in a dislocation may tend to relax into a straight segment, as indicated by the white arrows. This straightening of curved dislocation implies that the dislocations evolve towards a more stable configuration, possibly escaping from weaker pinning points along the dislocation line. All the dislocations moved in a similar way, and under the same loading the distance of their forward-march is larger in the first cycle after aging (Fig. 2d) compared with that in the last cycle before aging (Fig. 2a). This increased ease of movement is consistent with the trend in our measured critical activation stress in Fig. 1d, and with the straightening of curved dislocation segments. This experiment rules out the possibility that 'aging' in vacuum and in the presence of electron irradiation could cause pinning of the dislocation lines.

As the cycle number increases, the forward-and-back movements of the dislocations became more and more reversible. After repeating such dislocation movements for additional 95 cycles (Fig. 3a), we are now in the position to watch hydrogen effects. We stopped loading, waited $\sim$30 min in beam-off condition in vacuum, then started the hydrogenating process, which is a $\sim$30 min beam-on exposure to $\sim$2 Pa H_2. As seen in Fig. 3b,c, two minor changes can be observed by comparing the image before and after the hydrogenation: tiny blisters appeared on the pillar surface (as indicated by black arrows) and a short curved dislocation segment became straight (as indicated by the white arrow). The former unequivocally proves that hydrogen has been introduced into the aluminium pillar[29]. The latter, on the other hand, cannot be simply attributed to the effect of hydrogen, considering that straightening of dislocation also occurred in the previous vacuum aging experiment (Fig. 2b,c). By carefully examining this curved dislocation segment in Fig. 3b, a black pinning point can be found on the dislocation bow-out. It appears that it is the loss of this pinning point that allowed the dislocation to relax and become straight.

The key observation is that in the ensuing 85 loading cycles after hydrogenation, all five dislocations stood firm (Fig. 3d; Supplementary Movie 2), even though the loading conditions were exactly the same as that before the hydrogenation. Therefore, the critical stress to activate dislocation motion must be at least 250 MPa for all the five dislocations in the hydrogenated pillar. For dislocation #2, the critical stress is at least $\sim$150 MPa higher than, or 2.5$\times$ of, the last measured value (Fig. 1d) in vacuum tests. Since vacuum aging and e-beam irradiation only tend to facilitate dislocation motion (see earlier), the observed absence of dislocation motion is due to the effect of hydrogen, which we will refer to as 'hydrogen locking of dislocations'. The locking effect can be further corroborated by the higher critical stress for activating dislocation motion in another two different sets of experiments: monotonic compression tests (Supplementary Note 2; Supplementary Fig. 3) and bending of smooth cantilevers (Supplementary Note 3; Supplementary Fig. 4).

Later in the experiments these reactivated dislocations changed their profiles dramatically due to a drift of the loading punch, which induced buckling and exerted an additional stress on dislocations (Supplementary Note 4; Supplementary Fig. 5). The dislocation configuration inside the pillar was re-stabilized by continuing to cycle with a peak stress of $\sim$250 MPa for 81 cycles, and at this time only one long mobile dislocation was left. As shown in Fig. 4a, this dislocation does the same reversible movements for 186 cycles. These cycles are from 9 tests, and between each two successive tests there is a resting time of 2–5 min for tip realignment and sample characterization. It is surprising to observe that during these periods, hydrogen has never re-gathered to re-lock the dislocation to stop its subsequent motion, as shown in Fig. 4b.
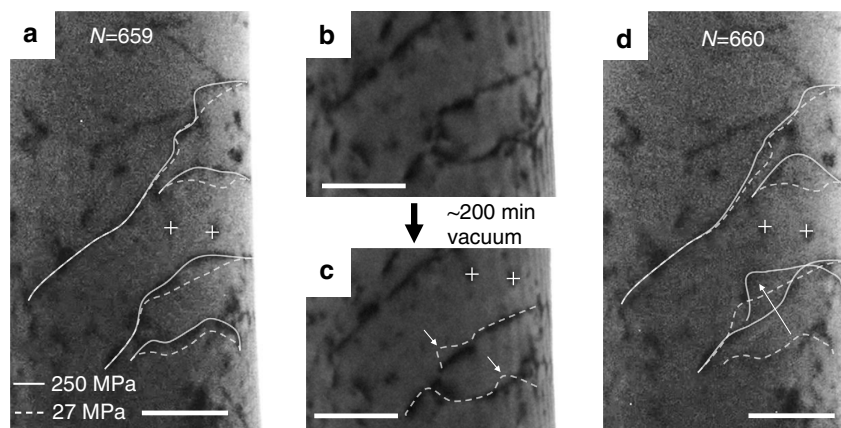

Figure 2 | The effect of vacuum aging on dislocation movements in hydrogen-free sample. (**a**) Dislocation motion in the cycle immediately before the vacuum aging. Dashed line and solid line indicate dislocation positions at the valley stress (27 MPa) and peak stress (250 MPa), respectively. (**b**) and (**c**) Dislocation configurations before and after vacuum aging, respectively, during which some of the defects disappeared and the curved dislocation segment tends to be straightened (marked with white arrow). (**d**) After 'aging' in vacuum for about 200 min at room temperature. All the moving dislocations continue to move in a similar way but to further distance. All scale bars are 200 nm.
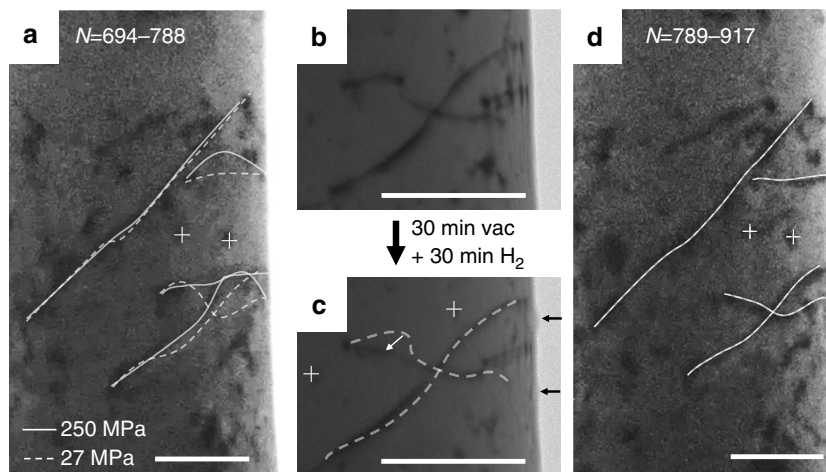
Figure 3 | Effect of hydrogenation on dislocation movements. (**a**) Dislocation response to cyclic loads before hydrogenation. All the four observed dislocations ceased their motion immediately after hydrogenation under the same loading stress. (**b**) and (**c**) Respective positions of the four mobile dislocations before and after the hydrogenation, during which a curved segment of dislocation was relaxed due to the loss of pinning point. Besides, tiny blisters appeared on the surface (marked with black arrows). Dislocation positions in (**b**) is superimposed onto (**c**) with white dashed line for reference. (**d**) Dislocation response to the same cyclic load after hydrogenation. All dislocations ceased their motion. All scale bars are 200 nm.
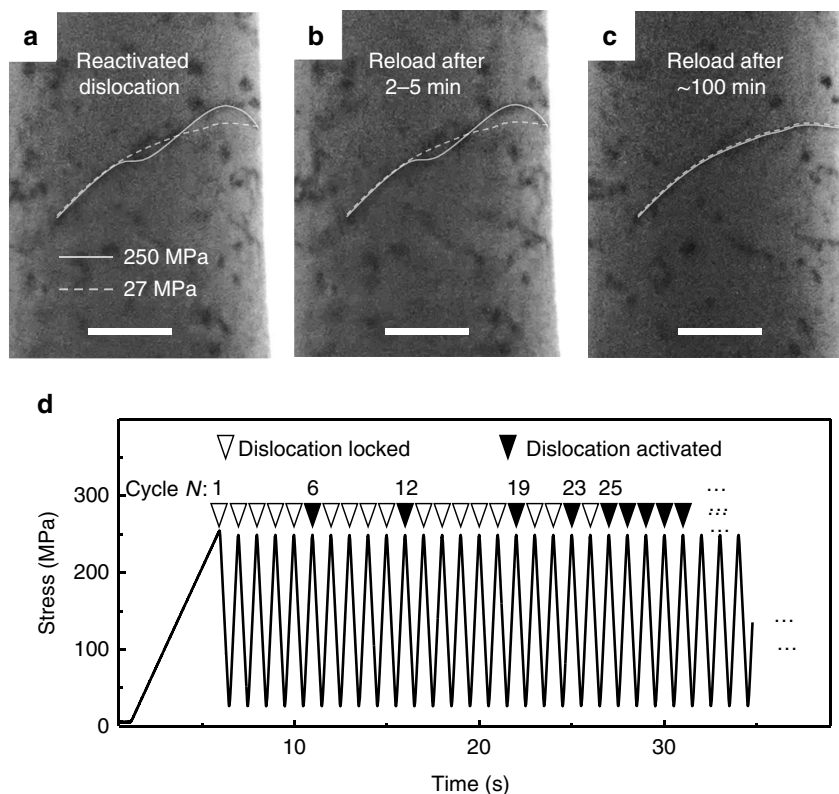

Figure 4 | Effect of Aging time on the dislocation motion in the hydrogenated pillar. (**a**) Dislocation configuration inside the hydrogenated pillar and its dislocation movements. (**b**) After 2~5 min aging periods, the dislocation continue moving in the same way. (**c**) After 100 min aging, the dislocation is relocked. (**d**) Dislocation movements after switching back to vacuum. The intermittent activation of dislocation motion shows an increasing chance of reoccurrence, as the hydrogen content diminishes with time. All scale bars are 200 nm.

The hydrogen gas was then cut off and the pillar was aged in vacuum for about 100 min, to allow the redistribution of the trapped hydrogen. After this step, the same cycling load was applied to the pillar (Supplementary Movie 3). It can be seen that the dislocation has been re-locked, as seen in the first few cycles in Fig. 4c. But in the following cycles, movement was initiated in a stick-slip manner, as marked by black triangles in Fig. 4d. The first movement happened in the sixth cycle of this test, but the

next movement happened six cycles later. As the cycle number increases, the intermittent dislocation movement becomes more and more frequent as the dislocation shed obstacles and eventually it turns into successive reciprocating motion in each cycle, for all cycles after $N = 25$.

To recapitulate, our cyclic compression tests above have provided clear evidence that dislocation locking will take place in the presence of H. However, the long diffusion time of a few

tens of minutes indicates that the observed locking effect is not from H interstitials acting alone. This conjecture arises because in some *in situ* TEM experiments, hydrogen introduction is reported to impact dislocation behaviour in less than one second[12,30]. The enthalpy of migration of hydrogen interstitial in aluminium is estimated to be only about 0.19 eV (refs 31,32); this translates into reaching equilibrium within one second in a sub-micron sample. Such hydrogen diffusion times are at least three orders of magnitude less than that in our experimental observation. Therefore, the strong locking of dislocations should involve other forms of point defects. As mentioned before, superabundant vacancies are likely preserved inside metals, no matter whether the hydrogen charging methods are chemical, electrochemical or plasma based[16,33]. In our experiments, the incident electron beam interacts with and ionize the hydrogen gas. The produced free hydrogen atoms and ions make the local environment quite similar to the hydrogen plasma reported by Buckley *et al.*[16], such that after hydrogen exposure there should be superabundant vacancies inside the aluminium pillar. The diffusion should then involve the migration of hydrogen-vacancy complexes, which are energetically more stable and also move much more sluggishly than hydrogen interstitials[34–36]. Such gas-stabilized vacancies and cavities are indeed well known in radiation damage[37], which also cause plastic flow localization and embrittlement. Therefore, we propose that it is the segregation of hydrogenated vacancy to the dislocation core that has resulted in the observed dislocation locking.

Atomistic simulations. Earlier density functional theory calculations have shown that the binding energy of one H interstitial and one vacancy (Va) is around 0.4 eV (ref. 38), which indicates that the hydrogen-vacancy (VaH) complex is relatively stable. Based on a Al-H angular-dependent potential (ADP)[39] (see Methods and Supplementary Note 5 for the evaluation of this potential), we calculated the migration paths of hydrogen and hydrogen-vacancy complex by using the climbing image nudged elastic band method[40], as shown in Fig. 5a. In comparison with the barrier of 0.19 eV for H interstitial diffusion, a VaH complex needs to overcome a much higher barrier of 0.67 eV. We can then obtain the diffusion coefficient of the VaH complex at room temperature as $D = D_0 \exp(-E^m/k_B T) \approx 2.8 \times 10^{-14}\,\mathrm{cm^2\,s^{-1}}$, where $D_0 = 5.9 \times 10^{-7}\,\mathrm{m^2\,s^{-1}}$ (ref. 41), E^m is the diffusion barrier, k_B is Boltzmann constant and T is absolute temperature. In agreement with this, the diffusivity of hydrogen–vacancy complexes was reported to be of the magnitude of $10^{-15}\,\mathrm{cm^2\,s^{-1}}$ in pure aluminium[16,31]. Finally, we can estimate the time scale for the hydrogen–vacancy complex to diffuse from the surface to the centre of pillar, $t = r^2/4D$, where r is the pillar radius (300 nm). The diffusion time required is ~120 min at room temperature; this is consistent with the locking time scale seen in our experiments.

In comparison to that of hydrogen interstitials (Supplementary Note 6; Supplementary Figs 6–7), we further simulate the effect of hydrogen-vacancy complexes on the critical stress of dislocation motion (Supplementary Note 7; Supplementary Figs 8–9). Figure 5b shows the configurations of edge dislocation core decorated with hydrogen interstitials and hydrogen–vacancy complexes, respectively. The hydrogen interstitials do not change the core structure of dislocation very much, while hydrogen–vacancy complexes can form dislocation jogs. Figure 5c shows the shear stress-strain curves for pure Al, Al–H, and Al–VaH systems, under the same level of segregation with one H (or VaH) per nanometre in the dislocation line. Compared with pure Al, a higher shear stress (~32 MPa) is required for driving dislocation motion, indicating that hydrogen interstitials take
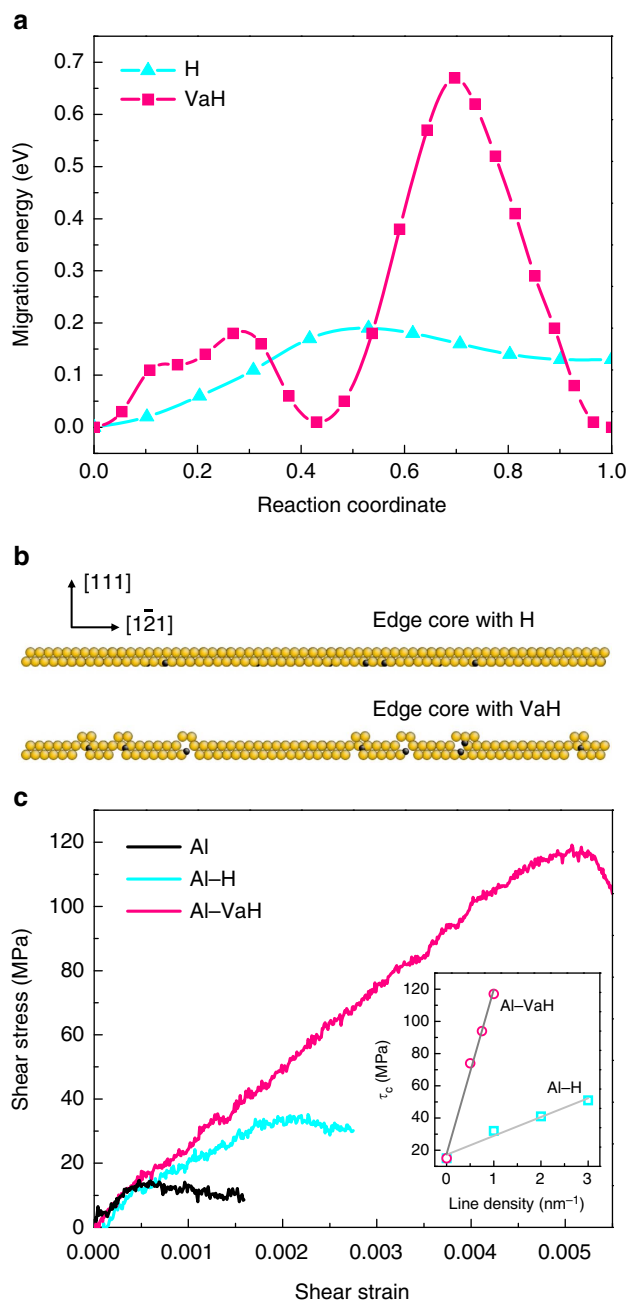

Figure 5 | Atomistic simulation of the pinning effect of hydrogen-vacancy complexes on dislocation motion. (**a**) Migration paths of hydrogen (H) from one tetrahedral (T) interstitial site to the neighbouring octahedral (O) site, and hydrogen-vacancy (VaH) complexes in aluminium. (**b**) Side view of dislocation core decorated by hydrogen and hydrogen-vacancy complex, respectively. Atoms with golden and black colours refer to aluminum and hydrogen, respectively. (**c**) The shear stress-strain curves of different systems. The density of hydrogen and hydrogen-vacancy complexes along dislocation line is one per nanometre. The inset shows the dependence of critical shear stress (τ_c) on the concentration of hydrogen and hydrogen-vacancy complexes. The linear fitting is made for both systems.

certain pinning effect on dislocation motion. In contrast, for Al–VaH, the critical shear stress (~117 MPa) is even much higher than that for Al–H. This suggests a much stronger locking effect from VaH. Our recent studies also showed that the hydrogen–vacancy complex roots very stably in the lattice when

meeting dislocations in BCC α-Fe (ref. 18), instead of being picked up and swept away by the moving dislocation. Here the simulations in Al further confirm that such complex can hinder dislocation motion strongly in FCC metals. Moreover, the critical shear stress (τ_c) for dislocation motion is found to increase linearly with the concentration of hydrogen and hydrogen-vacancy complexes along the dislocation core (inset in Fig. 5c), and in the case of hydrogen–vacancy complex shows a much steeper slope.

Discussion

Evidence of intense dislocation activity can be found in many metals that show macroscopic HE, at least locally at $\sim 10^2$ nm length scale beneath the fracture surface[10,20]. Stress-driven dislocation activities, such as intersecting of two dislocations, are known to produce excess vacancies atomically (now further stabilized by H)[18,20], forming a feedback loop of ever-more intense localization. In non-hydride-forming metals, hydrogen-enhanced localized plasticity (HELP)[11,42] as a descriptive mechanism finds widespread support. According to the HELP theory of HE (ref. 10), plastic localization happens first, and main material damage happens later[20], in a fashion like ductile failures in metals without hydrogen, but within a reduced space-time volume, giving rise to reduced fracture toughness overall. Plastic localization requires microscopic mechanisms for softening and/or flow planarization. While not addressing the entire question, we note certain parallels between what we see in our ETEM measurements, namely VaH locking and time-dependent stress-driven unlocking of dislocation, and strain aging induced plastic flow localization. So while a concentrated VaH atmosphere hardens the material initially, it also sets it up for a potentially dramatic softening later, if the dislocation cores shake free of the segregated VaH by moving long enough distances without stopping, which we have directly seen in our ETEM experiment. This dynamic softening is expected to be the most active near a macro-crack tip, where the tensile triaxial stress is the greatest to attract the largest hydrogen background concentration. So strain aging induced plastic localization instability may occur in hydrogen-charged metal[43,44], due to the hysteretic dislocation motion. Once an initial strain-softening and plastic localization length scale is established, the stored elastic energies of the surrounding materials will be dumped into this zone, greatly accelerating material damage accumulation in the forms of more hydrogenated vacancies and cavities[18,20], cracking of interfaces, etc. which may activate secondary mechanisms of softening and further localization, until the damaged material (defined by reduced total metal–metal coordination number) is localized to sharper and sharper zones, ultimately turning into two topologically separate surfaces. Our finding of time-dependent dislocation locking/unlocking due to hydrogen-vacancy complexes, observed at individual dislocation level in ETEM, sheds light on the initiation and feedback mechanisms of HELP and HE in non-hydride-forming metals. It likely also has bearing on subsequent damage accumulation, since vacancy is the smallest unit of structural damage as measured by reduction of total metal–metal coordination (for example gas-stabilized vacancies and cavities are basic forms of radiation damage[37]), a supersaturation of which can be easily generated by the plethora of dislocation intersections in a region with heavy plastic deformation[18,20].

Methods

Sample preparation. Single crystal aluminium (99.9995%) disks were cut into 1.5×2 mm^2 rectangular plates, which were mechanically polished to 100 μm in thickness and electrochemically thinned to a few microns at one edge. Submicron-sized cylindrical pillars were prepared by Focused ion beam (FIB, FEI Helios

NanoLab 600, operating at 30 keV) milling on the thinned edge. The used milling current in the last step was as low as ~ 20 pA to minimize geometrical taper and irradiation damage induced by ion beam. The thickness of surface affected layers were about 7 nm according to the TEM observation. All pillars had a taper of $\sim 2.5°$ and an aspect ratio (top diameter/length) of $\sim 1/3$.

In situ mechanical tests. The in situ TEM nanocompression tests were performed using a Hysitron PI95 H1H PicoIndenter. Pillars were loaded using a diamond punch, which was connected to a MEMS transducer with force resolution of ~ 300 nN and displacement resolution of ~ 2 nm. Both the loading direction and electron-beam direction were $\langle 110 \rangle$ direction for all the tested pillars (Supplementary Fig. 1). A pillar of 620 nm in top diameter was used for cyclic compression test. A carbon cap layer of 100 nm in thickness was deposited atop the aluminium by ion beam assisted deposition under beam current of 18 pA, as shown in Fig. 1a. This cap layer has low adhesion force to the diamond punch and can help to maintain a stable contact between the punch and pillar during multiple tests. At the same time, this cap layer can act as a buffer layer, which can help avoid unnecessary dislocation emission from the top surface by eliminating stress singularities, so that dislocation configuration inside the pillar can remain undistracted after many tests.

We used load control since the feedback control can automatically compensate for the displacement drift in the loading direction and assure that all cycles reach almost the same peak stress. The whole experiment consists of 21 loading sessions, and each loading session has 6–99 cycles, of which the leading cycle is 5 s (4.5 s loading + 0.5 s unloading) and all the trailing cycles are 1 s per cycle (0.5 s loading + 0.5 s unloading). In total, 1414 cycles were applied to the sample. During cyclic compression, the loading stress oscillates between valley stress (25–30 MPa) and peak stress (~ 250 MPa), as shown in Fig. 2b. The first 339 cycles use peak stress of ~ 330 MPa to mechanically decrease the dislocation density, and all the other cycles have peak stress of ~ 250 MPa to manipulate the movements of the few mobile dislocations left.

Real-time observation was conducted in an environmental TEM (Hitachi H9500, operating at 300 kV and 1 μA emission current). The compression tests were carried out subsequently in vacuum and ~ 2 Pa pure hydrogen gas. Before the tests in hydrogen environment, samples were hydrogenated under electron-beam intensity of ~ 0.45 nA μm^{-2} in ~ 2 Pa H$_2$ for about 30 min, which is long enough for hydrogen diffusion while not too long to cause obvious blistering on the pillar surface[29]. The dislocations inside the pillar roughly keep the same configuration during the charging process. And the following mechanical tests were performed in the same hydrogen atmosphere but with much lower beam intensity (~ 0.05 nA μm^{-2}).

Atomistic simulations. The interatomic interaction in Al–H system is described by an angular dependent empirical potential[39]. This potential reproduces many properties quite well, especially the energetics related to the point defects such as hydrogen dissolution energy, hydrogen migration energy and so on, but it underestimates the binding energy of hydrogen–vacancy complex (Supplementary Note 5; Supplementary Tables 1–3). To address the kinetic properties of the H and VaH complex, the migration barriers and paths were calculated by using the climbing image nudged elastic band[40] method. We further studied the locking effect that hydrogen or hydrogen-vacancy complexes exert on dislocation motion. Although the binding energy of VaH is underestimated by ADP potential, we did not use the ADP to calculate H, Va and VaH partition in H + Va = VaH. We simply placed VaH complexes inside the dislocation core, and study their dragging effect on the dislocation. For this particular calculation, the binding energy of H with Va to form VaH is mostly irrelevant. The binding energy of the dislocation core with VaH is more important.

For the simulations, we first created an $a/2\langle 110 \rangle$-type edge dislocations in Al. The simulation box was oriented along x-[10$\bar{1}$], y-[111], z-[12$\bar{1}$], with dimensions of $23 \times 28 \times 16$ nm^3. Periodic boundary conditions were applied in the x and z directions. A certain amount of hydrogen atoms or hydrogen-vacancy complexes were then introduced in the region around the dislocation core regime according to the Boltzmann occupation probability. The system was further relaxed at 300 K for 100 ps using a Nosé-Hoover thermostat[45]. Finally shear strain was applied in the xz-plane to drive dislocation glide along the x direction. The strain rate was on the order of 10^8 s^{-1}. The whole calculations were carried out using the LAMMPS (ref. 46) code and the atomic configurations were displayed via AtomEye[47]. The details of model construction and simulation procedure are shown in Supplementary Notes 6 and 7.

Data availability. The data that support the findings of this study are available from the corresponding authors on request.

References

1. Johnson, W. H. On some remarkable changes produced in iron and steel by the action of hydrogen and acids. *Proc. R. Soc. Lond.* **23,** 168–179 (1874).
2. Kimura, H. & Matsui, H. Mechanism of hydrogen-induced softening and hardening in iron. *Scr. Metall.* **21,** 319–324 (1987).
3. Zhao, Y. *et al.* The role of hydrogen in hardening/softening steel: Influence of the charging process. *Scr. Mater.* **107,** 46–49 (2015).

4. Miresmaeili, R., Liu, L. J. & Kanayama, H. A possible explanation for the contradictory results of hydrogen effects on macroscopic deformation. *Int. J. Pres. Ves. Pip.* **99,** 34–43 (2012).

5. Hirth, J. P. Effects of hydrogen on the properties of iron and steel. *Metall. Trans. A* **11,** 861–890 (1980).

6. Lynch, S. P. in *Gaseous hydrogen embrittlement of materials in energy technologies* Vol. 2 (eds Gangloff, R. P. & Somerday, B. P.) Ch. 9, 274–346 (Woodhead Publishing, 2012).

7. Murakami, Y. & Matsuoka, S. Effect of hydrogen on fatigue crack growth of metals. *Eng. Fract. Mech.* **77,** 1926–1940 (2010).

8. Martin, M. L., Fenske, J. A., Liu, G. S., Sofronis, P. & Robertson, I. M. On the formation and nature of quasi-cleavage fracture surfaces in hydrogen embrittled steels. *Acta Mater.* **59,** 1601–1606 (2011).

9. Cottrell, A. H. & Bilby, B. A. Dislocation theory of yielding and strain aging of iron. *Proc. Phys. Soc. Lond. Sect. A* **62,** 49–62 (1949).

10. Robertson, I. et al. Hydrogen embrittlement understood. *Metall. Mater. Trans. B* **46,** 1085–1103 (2015).

11. Robertson, I. M. The effect of hydrogen on dislocation dynamics. *Eng. Fract. Mech.* **68,** 671–692 (2001).

12. Bond, G. M., Robertson, I. M. & Birnbaum, H. K. Effect of hydrogen on deformation and fracture processes in high-purity aluminium. *Acta Metall.* **36,** 2193–2197 (1988).

13. Song, J. & Curtin, W. A. Mechanisms of hydrogen-enhanced localized plasticity: an atomistic study using α-Fe as a model system. *Acta Mater.* **68,** 61–69 (2014).

14. Song, J. & Curtin, W. Atomic mechanism and prediction of hydrogen embrittlement in iron. *Nat. Mater.* **12,** 145–151 (2013).

15. Buckley, C. E. et al. Characterization of H defects in the aluminium-hydrogen system using small-angle scattering techniques. *J. Appl. Crystallogr.* **34,** 119–129 (2001).

16. Buckley, C. E. & Birnbaum, H. K. Characterization of the charging techniques used to introduce hydrogen in aluminum. *J. Alloy. Compd.* **330,** 649–653 (2002).

17. Fukai, Y. Superabundant vacancies formed in metal-hydrogen alloys. *Phys. Scr.* **T103,** 11–14 (2003).

18. Li, S. et al. The interaction of dislocations and hydrogen-vacancy complexes and its importance for deformation-induced proto nano-voids formation in α-Fe. *Int. J. Plast.* **74,** 175–191 (2015).

19. Nagumo, M. Hydrogen related failure of steels - a new aspect. *Mater. Sci. Technol.* **20,** 940–950 (2004).

20. Neeraj, T., Srinivasan, R. & Li, J. Hydrogen embrittlement of ferritic steels: Observations on deformation microstructure, nanoscale dimples and failure by nanovoiding. *Acta Mater.* **60,** 5160–5171 (2012).

21. Momida, H., Asari, Y., Nakamura, Y., Tateyama, Y. & Ohno, T. Hydrogen-enhanced vacancy embrittlement of grain boundaries in iron. *Phys. Rev. B* **88,** 144107 (2013).

22. Takai, K., Shoda, H., Suzuki, H. & Nagumo, M. Lattice defects dominating hydrogen-related failure of metals. *Acta Mater.* **56,** 5158–5167 (2008).

23. Hatano, M., Fujinami, M., Arai, K., Fujii, H. & Nagumo, M. Hydrogen embrittlement of austenitic stainless steels revealed by deformation microstructures and strain-induced creation of vacancies. *Acta Mater.* **67,** 342–353 (2014).

24. Doshida, T., Nakamura, M., Saito, H., Sawada, T. & Takai, K. Hydrogen-enhanced lattice defect formation and hydrogen embrittlement of cyclically prestressed tempered martensitic steel. *Acta Mater.* **61,** 7755–7766 (2013).

25. Scully, J. R., Young, Jr. G. A. & Smith, S. W. Hydrogen solubility, diffusion and trapping in high purity aluminum and selected Al-base alloys. *Materials Science Forum* **331-337,** 1583–1600 (2000).

26. Fukai, Y. & Sugimoto, H. Formation mechanism of defect metal hydrides containing superabundant vacancies. *J. Phys. Condens. Matter* **19,** 436201 (2007).

27. Shan, Z. W., Mishra, R. K., Asif, S. A. S., Warren, O. L. & Minor, A. M. Mechanical annealing and source-limited deformation in submicrometre-diameter Ni crystals. *Nat. Mater.* **7,** 115–119 (2008).

28. Wang, Z.-J. et al. Cyclic deformation leads to defect healing and strengthening of small-volume metal crystals. *Proc. Natl Acad. Sci.* **112,** 13502–13507 (2015).

29. Xie, D. et al. *In situ* study of the initiation of hydrogen bubbles at the aluminium metal/oxide interface. *Nat. Mater.* **14,** 899–903 (2015).

30. Shih, D. S., Robertson, I. M. & Birnbaum, H. K. Hydrogen embrittlement of alpha-titanium - in situ TEM studies. *Acta Metall.* **36,** 111–124 (1988).

31. Young, G. & Scully, J. The diffusion and trapping of hydrogen in high purity aluminum. *Acta Mater.* **46,** 6337–6349 (1998).

32. Wolverton, C., Ozoliņš, V. & Asta, M. Hydrogen in aluminum: First-principles calculations of structure and thermodynamics. *Phys. Rev. B* **69,** 144109 (2004).

33. Birnbaum, H. K. et al. Hydrogen in aluminum. *J. Alloy. Compd.* **253–254,** 260–264 (1997).

34. Hebert, K. R. Trapping of hydrogen absorbed in aluminum during corrosion. *Electrochim. Acta* **168,** 199–205 (2015).

35. Ai, J. H. & Scully, J. R. Hydrogen diffusivity during corrosion of high-purity aluminum. *Corrosion* **69,** 752–767 (2013).

36. Gunaydin, H., Barabash, S. V., Houk, K. & Ozoliņš, V. First-principles theory of hydrogen diffusion in aluminum. *Phys. Rev. Lett.* **101,** 075901 (2008).

37. Ding, M. S. et al. Radiation-induced helium nanobubbles enhance ductility in submicron-sized single-crystalline copper. *Nano Lett.* **16,** 4118–4124 (2016).

38. Lu, G. & Kaxiras, E. Hydrogen embrittlement of aluminum: The crucial role of vacancies. *Phys. Rev. Lett.* **94,** 155501 (2005).

39. Apostol, F. & Mishin, Y. Angular-dependent interatomic potential for the aluminum-hydrogen system. *Phys. Rev. B* **82,** 144115 (2010).

40. Henkelman, G., Uberuaga, B. P. & Jonsson, H. A climbing image nudged elastic band method for finding saddle points and minimum energy paths. *J. Chem. Phys.* **113,** 9901–9904 (2000).

41. Ho, G., Ong, M. T., Caspersen, K. J. & Carter, E. A. Energetics and kinetics of vacancy diffusion and aggregation in shocked aluminium via orbital-free density functional theory. *Phys. Chem. Chem. Phys.* **9,** 4951–4966 (2007).

42. Birnbaum, H. K. & Sofronis, P. Hydrogen-enhanced localized plasticity–a mechanism for hydrogen-related fracture. *Mater. Sci. Eng. A* **176,** 191–202 (1994).

43. Wilcox, B. & Smith, G. The Portevin-Le Chatelier effect in hydrogen charged nickel. *Acta Metall.* **12,** 371–376 (1964).

44. Latanision, R. & Staehle, R. The effect of continuous hydrogenation on the deformation of nickel single crystals. *Scr. Metall.* **2,** 667–672 (1968).

45. Nosé, S. A unified formulation of the constant temperature molecular dynamics methods. *J. Chem. Phys.* **81,** 511–519 (1984).

46. Plimpton, S. Fast parallel algorithms for short-range molecular dynamics. *J. Comput. Phys.* **117,** 1–19 (1995).

47. Li, J. AtomEye: an efficient atomistic configuration viewer. *Model. Simul. Mater. Sci. Eng.* **11,** 173 (2003).

Acknowledgements

Author contributions

Z.S. and J.L. designed the project. D.X., M.L. and Z.W. conducted the experimental work. S.L., J.L. and P.G. performed the simulation work. D.X., S.L., J.L. and E.M. wrote the paper. All authors contributed to discussions of the results and revisions of the manuscript.

Additional information

1

Supplementary Figure 1. Process to achieve individual-dislocation configuration through small-strain-amplitude cyclic compression. (**a**) As-fabricated pillar contains high density of dislocations. (**b**) After 339 cycles of cyclic compression with peak stress of 330 MPa, the dislocation density dramatically decreased. (**c**) After another 355 cycles of cyclic compression with peak stress of 250 MPa, only a few long dislocations remained inside the pillar. (**d**) The diffraction pattern of the single crystal aluminum pillar, for which the loading axis is inclined to the [1$\bar{1}$0] direction by 7°. (**e**) Schematic of the mobile dislocations in (c) and one of the possible slip system, for which the Schmidt's factor M is calculated to be 0.070. All scale bars represent 200 nm.
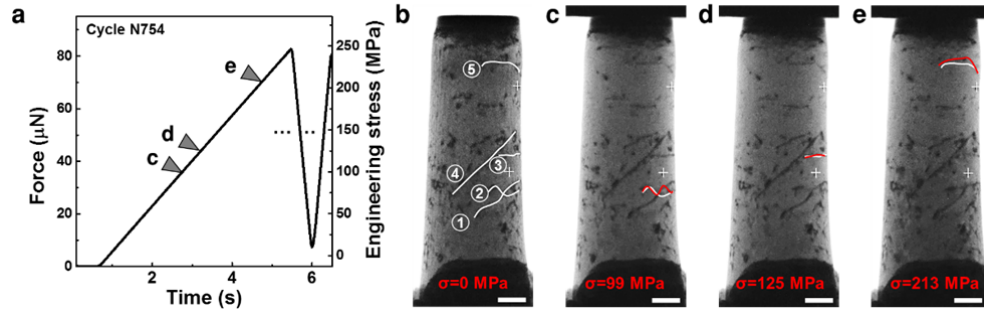
Supplementary Figure 2. The threshold loads for each dislocation determined in the first loading cycle in vacuum. (**a**) Load vs. time curve of the slow leading cycle. The triangular markers correspond to the threshold loads of each dislocation to be activated. (**b**) The original configuration of the dislocations in the pillar before loading. (**c**), (**d**), and (**e**) show the abrupt jump of dislocations #2, #3 and #5 at critical loading stresses of 99, 125, and 213 MPa respectively. The red lines and white lines are the dislocation profiles before and after the jump. For more details see supplementary Movie 1. All scale bars represent 200 nm.
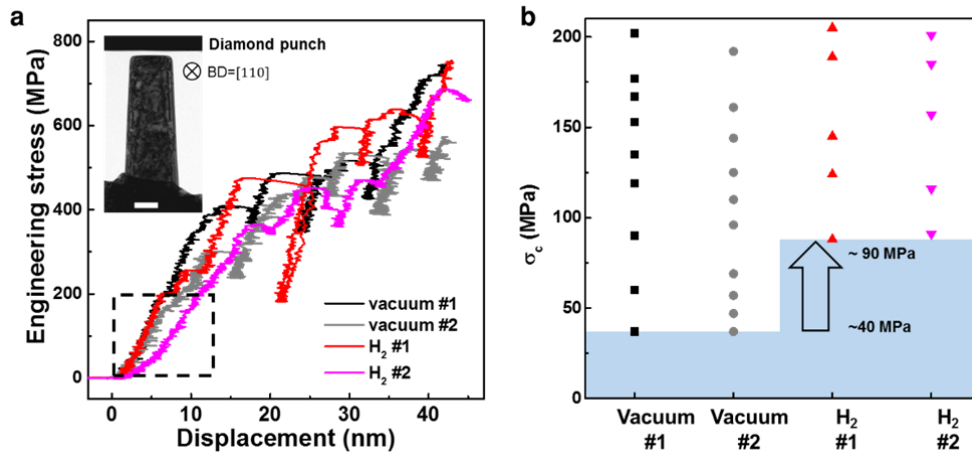
Supplementary Figure 3. Monotonic compression of aluminum pillars in vacuum and hydrogen gas. (**a**) Engineering stress-displacement curves showing similar yield stress and flow stress for tests in vacuum and in hydrogen. The inset illustrates the experimental setup. (**b**) The critical stress (σ_c) for dislocation depinning events in various samples, showing that a higher stress is required to set off dislocation motion in hydrogenated samples. Scale bar in inset in (a) is 200 nm.

29
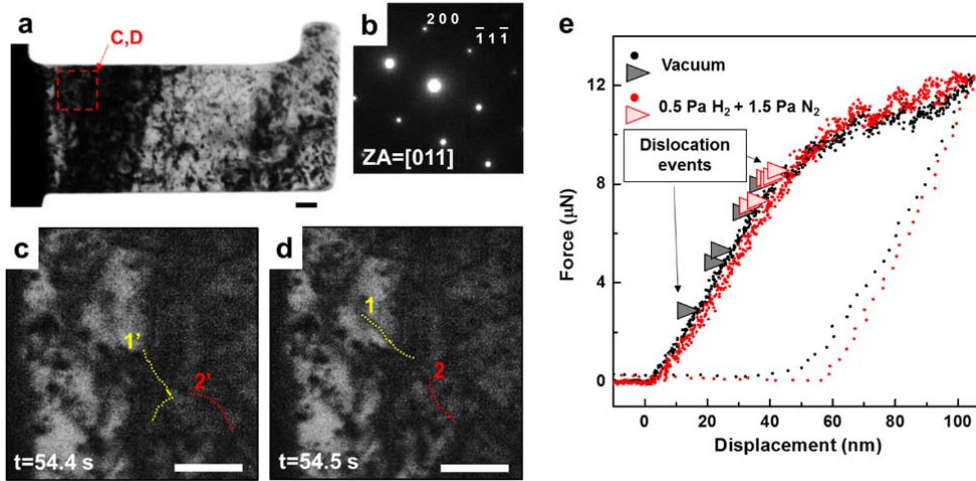
Supplementary Figure 4. Hydrogen effect on dislocation motion during bending tests. (**a**) Bright field TEM image of a typical bending cantilever containing dislocations and other defects. (**b**) The corresponding diffraction pattern showing the single crystal nature of the cantilever. (**c**) and (**d**) are the magnified area in (**a**) showing two typical dislocation profile at the given moments before and after sudden movements. (**e**) Force vs. displacement curves of two typical samples with similar dimensions but tested in vacuum and hydrogen environment, respectively. The first 5 dislocation events of each test are labeled on the curve with triangle marks. All scale bars represent 100 nm.
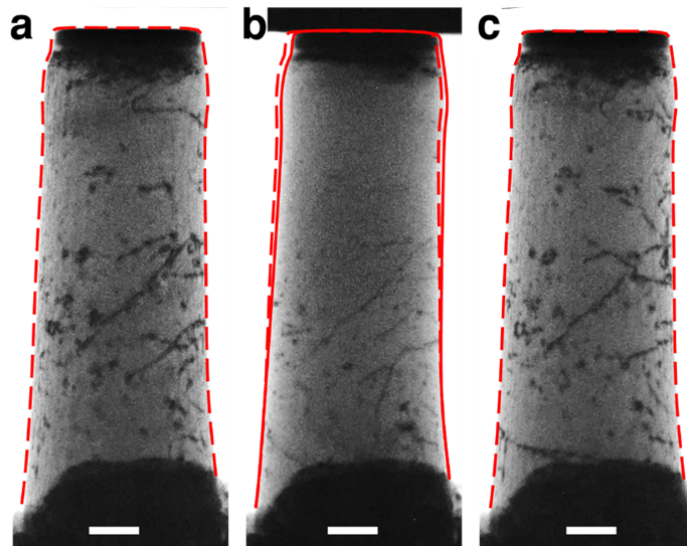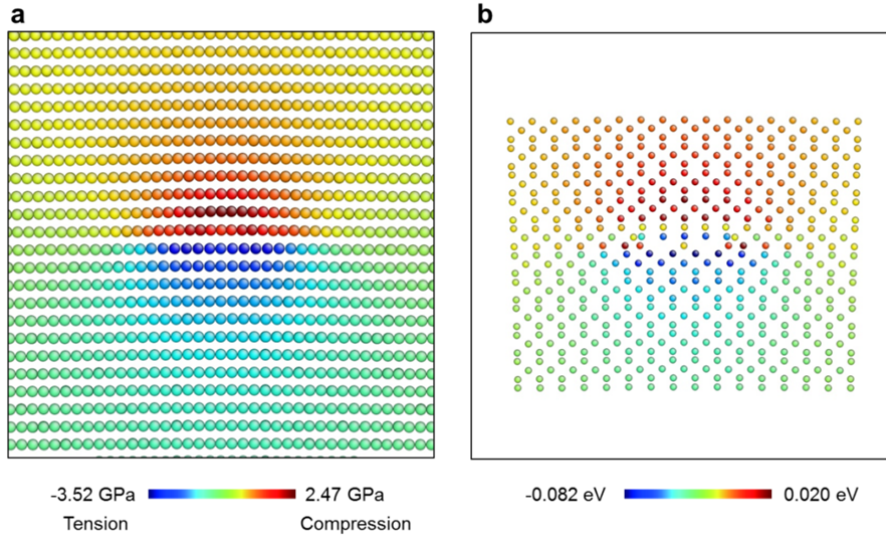
Supplementary Figure 5. Destruction of dislocation configuration due to bucking during the test in 2 Pa H_2. (**a**) The dislocation configuration inside the pillar remained unchanged after 85 cycles. (**b**) Due to the tip drift, the pillar was buckled. The dislocation configuration underwent a sudden change under the coupling of loading stress and buckling stress. Note pillar contour change before drift (red dashed line) and after drift (red solid line), as well as the change of black contrast inside the pillar due to buckling. (**c**) When the tip is detached from the pillar, the pillar contour recovered but the dislocation configuration can't be resumed. All scale bars represent 200 nm.

Tension / Compression color scales:
-3.52 GPa → 2.47 GPa (Tension — Compression)
-0.082 eV → 0.020 eV

Supplementary Figure 6. The distribution maps of (**a**) hydrostatic stress of edge dislocation in aluminum and (**b**) total energy difference of hydrogen ($\Delta E_{\text{H},i}$) in interstitial sites around the dislocation core. Generally, interstitial hydrogen in the region with minus hydrostatic stress (tension) has a smaller value of $\Delta E_{\text{H},i}$ and that in the region with positive hydrostatic stress (compression) has a larger value of $\Delta E_{\text{H},i}$. The tensile region around dislocation core corresponds to the most energy-favored sites for hydrogen atoms.

60
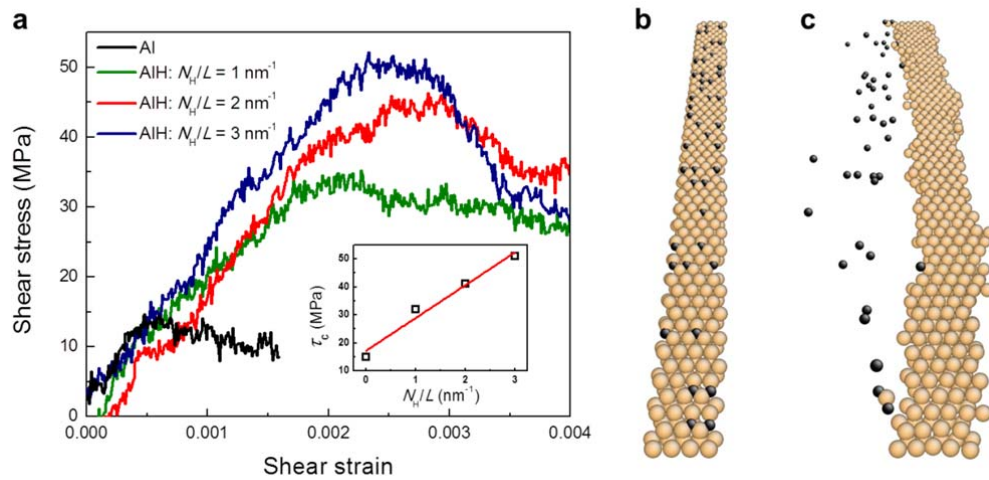
Supplementary Figure 7. Atomistic simulations based on the model with hydrogen atoms in a Boltzmann distribution. (**a**) Stress-strain curves at different hydrogen concentration levels. The critical shear stress (τ_c) for dislocation motion shows a linear increase with the increase of hydrogen concentration (N_H/L), as shown in the inset. (**b**) Initial configuration of dislocation decorated with hydrogen atoms. (**c**) The configuration at the depinning state. Atoms with golden and black colors refer to aluminum and hydrogen.

67

-3.52 GPa ▬▬▬▬▬ 2.47 GPa

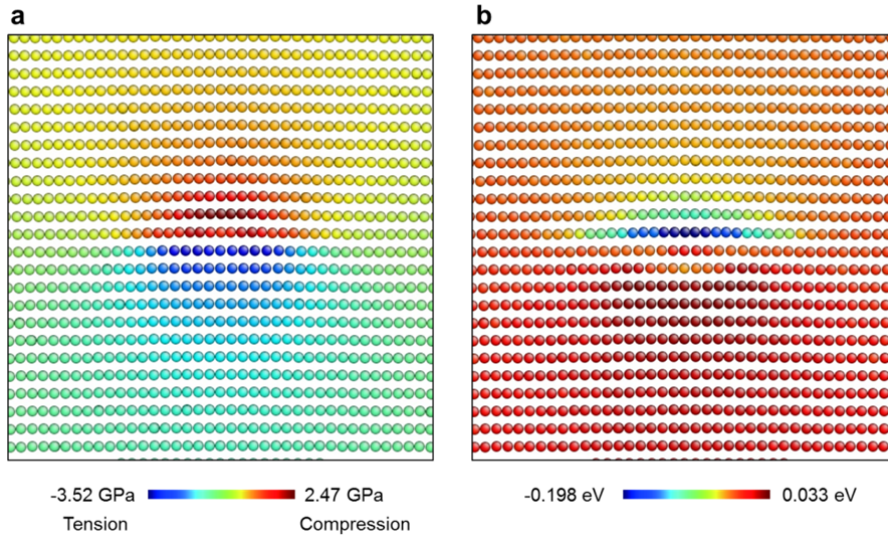Tension · Compression

-0.198 eV ▬▬▬▬▬ 0.033 eV

Supplementary Figure 8. The distribution maps of (**a**) hydrostatic stress of edge dislocation in aluminum and (**b**) total energy difference of VaH complex ($\Delta E_{\text{VaH},i}$) in site i ($E_{\text{VaH},i}^{\text{Edge}}$) with reference to that in bulk site ($E_{\text{VaH},i}^{\text{Bulk}}$).
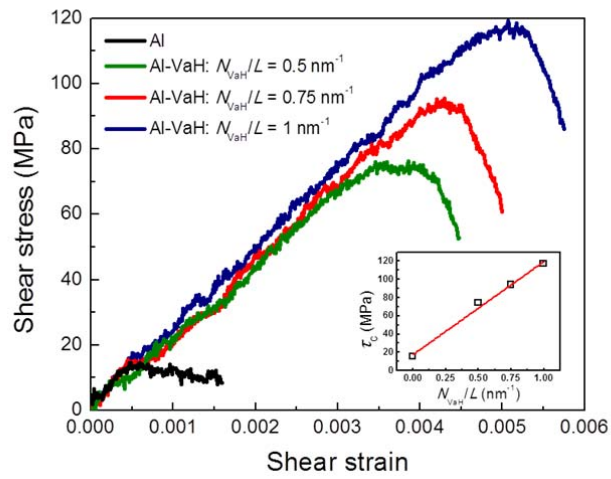
Supplementary Figure 9. MD simulations of dislocation pinning effect by hydrogen-vacancy complex. The different colored lines show the stress-strain curves at different concentrations of hydrogen-vacancy complex. The critical shear stress (τ_c) for dislocation motion shows a linear increase with the increase of hydrogen-vacancy complex concentration (N_{VaH}/L), as shown in the inset.

80 **Supplementary Table 1.** Energetics of isolated H atom in Al. ΔE_s refers to the solution energy of
81 H in Al. T and O refer to the tetrahedral (T) interstitial and octahedral (O) interstitial sites. E_m
82 refers to the migration barrier of one H atom from a T-site to the O-site. The units are in eV.

	ADP	ab initio
ΔE_s (T)	0.69	0.69 (ref. 1)
ΔE_s (O)	0.82	0.82 (ref. 1)
E_m	0.19	0.18 (ref. 1)

83

84

85

86 **Supplementary Table 2.** Energetics of Va in Al. E_v^f refers to the vacancy formation energy and E_m
87 refers to the vacancy migration barrier. The units are in eV.

	ADP	Experiments
E_v^f	0.68	0.69 (ref. 2)
E_m	0.64	0.65 (ref. 3)

88

89

90

91 **Supplementary Table 3.** Energetics of VaH. E_f (T-Va) refers to the formation energy of vacancy
92 with H in T-site. E_f (O-Va) refers to the formation energy of vacancy with H in O-site. E_b (T-Va)
93 refers to the binding energy of vacancy with H in T-site. The units are in eV.

	ADP	ab initio
E_f (T-Va)	1.32	1.0 (ref. 4)
E_f (O-Va)	1.36	1.14 (ref. 4)
E_b (T-Va)	0.048	0.39 (ref. 5)

94

95

Supplementary Note 1: <u>Mechanical annealing by cyclic compression</u>

The loading function consists of a slow leading cycle and tens of fast trailing cycles in each group of test. In the loading half-cycle, each dislocation marches forward, like a bending bow, with both ends pinned on surface; upon unloading, each swings back to the original location (see supplementary Movie 1).

The initial compression tests were conducted with peak stress of ~330 MPa. By the end of 339th cycle (N339), only a few isolated mobile dislocations were left, with their both ends pinned by the surface of the sample (Supplementary Fig. 1b). In order to stabilize these dislocations further, we purposely lowered the peak stress down to ~250 MPa. A steady dislocation configuration was reached at N694 (Supplementary Fig. 1c), i.e. for each following cycle, the bow out extent of each dislocation remained the same at each peak stress.

In Supplementary Fig. 2, three dislocations show abrupt position change during the loading, whereas the two other dislocations only show smooth position change. Critical loading stress for dislocation #1, #3, and #5 are 99 MPa, 125 MPa, and 213 MPa respectively.

Supplementary Note 2: <u>Monotonic compression</u>

Four typical engineering stress-strain curves from monotonic compression tests are shown in Supplementary Fig. 3. Before the stress reaches 200 MPa, the curve looks linear without obvious yielding or strain burst. But when correlated with the movie frames, discrete movements of preexisting dislocations can be observed. These preexisting dislocations in the as-fabricated pillars mainly result from FIB damage in the milling process, and are pinned by obstacles such as surface junctions, point defects and other dislocations. As the applied load increases, dislocations start breaking away from pinning points, exhibiting abrupt movements. After depinning,

they either vanish at surfaces or get stopped at a stronger pinning point. We have tracked all the observed depinning events and their corresponding critical stresses, and found that the lowest depinning stress increases from ~40 MPa to ~90 MPa when changing the testing environment from vacuum to the 2 Pa hydrogen gas, as demonstrated in Supplementary Fig. 3b.

From the engineering stress-displacement curves, monotonic compressions in hydrogen environment show similar stiffness and strain hardening behavior when compared to compressions in vacuum. In these tests, the profile of stress-strain curve is mainly governed by sample-size dependent dislocation nucleation and multiplication. In Supplementary Fig. 3a, H_2 #2 specimen show lower stiffness than the other three pillars due to the slight misalignment and initial point contact at the beginning of the compression test.

Supplementary Note 3: <u>Hydrogen effect on dislocation motion in bending tests</u>

8 smooth cantilevers with width ranging from 222 nm to 292 nm and thickness from 600 nm to 642 nm were bent inside the ETEM. All the cantilevers (e.g. Supplementary Fig. 4a) contained preexisted dislocations resulting mainly from FIB milling. The dislocation density was estimated to be between 10^{13} m^{-2} and 10^{14} m^{-2}. Monotonic bending loads were applied to the cantilevers at loading rate of 5 nm/s under displacement control mode. Total 8 samples were tested, 4 in vacuum and 4 in hydrogen environment. Similar to that observed in monotonic compression tests (Supplementary Fig. 3), the threshold loads for dislocation activation in the hydrogen atmosphere are always higher than those tested in vacuum. One typical comparison is shown in Supplementary Figure 4e. It again demonstrates that hydrogen can improve the threshold loads significantly for those preexisted dislocations.

Supplementary Note 4: <u>**Reconfiguration of dislocations due to buckling/bending**</u>

<u>**induced by probe drift**</u>

150 Since a typical cyclic loading test lasts 40 to 100 seconds, the diamond punch may

151 undergo obvious drift in all three space coordinate directions. Under the load control

152 system, drift in the indentation direction can be automatically compensated by the

153 feedback control system so as to ensure a correct loading force applied to the pillar.

154 However, drifts perpendicular to the indentation axis can buckle the samples

155 obviously due to the friction confinement at the contact interface between the

156 diamond tip and the samples. This will apply addition stress to the dislocations. One

157 typical example is shown in Supplementary Fig. 5. The sample was bended/buckled

158 obviously (Supplementary Fig. 5b) during the cyclic loading, as suggested by the

159 profile deviation (red dashed lines) and the significant contrast change. New

160 dislocations coming out from the bottom disrupted the dislocation configuration

161 inside the pillar. Interestingly, the sample can go back to its original position after the

162 diamond probe was retracted despite that the dislocation configurations had been

163 dramatically changed.

164

165 **Supplementary Note 5:** <u>**Evaluation of Al-H angular dependent potential**</u>

166 To provide more details about the empirical angular-dependent potential (ADP)[6] we

167 used in MD simulations, here we show various properties predicted by this potential

168 in comparison to the experiments and ab initio calculations, especially some

169 energetics related to the point defects (H, Va and VaH), as shown in the following

170 three Tables 1, 2 and 3. Among them, most has a relatively good match with the

171 referenced data, but unfortunately, the binding energy of VaH is very small. More

172 information for this potential is shown in refs 6, 7.

173

Supplementary Note 6: Molecular dynamics simulation of the influence of

       hydrogen atmosphere on dislocation motion

We first created the $a/2<110>$-type edge dislocations in Al. The simulation box was oriented along x-$[10\bar{1}]$, y-$[111]$, z-$[1\bar{2}1]$, with dimensions of 23nm × 28nm × 16nm. Periodic boundary conditions were applied in the x and z directions. The hydrogen atoms were then introduced in the interstitial tetrahedral sites around the dislocation according to the Boltzmann occupation probability

$$p_{\mathrm{H},i} = e^{\Delta E_{\mathrm{H},i}/k_{\mathrm{B}}T} / \sum_{i} e^{\Delta E_{\mathrm{H},i}/k_{\mathrm{B}}T} \tag{S1}$$

where $\Delta E_{\mathrm{H},i}(= E_{\mathrm{H},i} - E_{\mathrm{H},i}^{\mathrm{Bulk}})$ is the total energy difference of hydrogen in site i ($E_{\mathrm{H},i}$) with reference to that in bulk tetrahedral interstitial site ($E_{\mathrm{H},i}^{\mathrm{Bulk}}$), k_{B} is Boltzmann constant and T is absolute temperature. Supplementary Fig. 6a shows the distribution of hydrostatic stress of the edge dislocation and Supplementary Fig. 6b shows the distribution of $\Delta E_{\mathrm{H},i}$ in tetrahedral site around the dislocation core. We can see that the two maps match relatively well. The tensile region corresponds to a much lower energy state, where most of the hydrogen atoms distribute. The most energy-favored sites for hydrogen are right in the dislocation core region. The hydrogen concentration around dislocation line is characterized with N_{H}/L, where N_{H} is the number of hydrogen atoms and L is the length of the dislocation line[8]. After adding hydrogen atoms, the system was further relaxed at 300 K for 100 ps using a Nosé-Hoover thermostat[9, 10]. Finally shear strain was applied in the xz-plane to drive dislocation glide along the x direction. The strain rate was on the order of 10^{8} s^{-1}. The whole calculations were carried out using the LAMMPS code[11] and the atomic configurations were displayed via AtomEye[12].

Supplementary Fig. 7a shows the shear stress-strain curves for Al-H system in comparison to H-free system at 300 K. An obvious locking effect can be observed: the

value of critical shear stress for edge dislocation motion increases in hydrogen environment. The dependence of locking strength on hydrogen concentration is studied by conducting a serial of simulations with different N_H/L. The inset in Supplementary Fig. 7a shows the variation of critical shear stress (τ_c) with different amount of N_H/L. We find that the value of τ_c increases almost linearly with hydrogen concentration as

$$\tau_c = \tau_0 + \alpha N_H / L \tag{S2}$$

where τ_0 (= 15 MPa) is the critical shear stress for dislocation motion without hydrogen and the coefficient α is 11.7 MPa·nm in the present Al-H system. It is interesting to observe that even hydrogen with a density of $N_H/L = 1$ nm^{-1} could double the τ_c. Supplementary Fig. 7b shows the initial configuration of dislocation decorated with hydrogen atoms at the level of $N_H/L = 3$ nm^{-1}. When the shear stress reaches the critical value, the dislocation suddenly escapes from the hydrogen atmosphere, as illustrated in Supplementary Fig. 7c.

Our MD simulations reveal in a straightforward manner that hydrogen atoms could enhance the critical stress for dislocation motion. The interaction between dislocation and diffusing solute hydrogen atoms can lead to locking effect, similar to that in strain aging[13, 14].

Supplementary Note 7: <u>Molecular dynamics simulation of the influence of</u>

<u>hydrogen-vacancy complexes on dislocation motion</u>

Our simulations above show that the hydrogen atoms themselves can take the pinning effect on dislocation motion. However, as we mentioned in the manuscript, the aging experiments show that the relocking needs a long time beyond hydrogen diffusion time. It is reasonable to speculate that there are some other obstacles to lock dislocations. By calculating the migration energy and estimating the diffusion length, we found that the most probable candidate is hydrogen-vacancy complex. In the

following, another set of simulations was performed to reveal the role of hydrogen-vacancy complex on dislocation motion. Similar to that in Al-H system, we introduced the VaH complexes according to the Boltzmann occupation probability

$$p_{\text{VaH},i} = e^{\Delta E_{\text{VaH},i}/k_{\text{B}}T} / \sum_i e^{\Delta E_{\text{VaH},i}/k_{\text{B}}T} \tag{S3}$$

where $\Delta E_{\text{VaH},i}$ is the total energy difference of VaH complex in site i ($E_{\text{VaH},i}$) with reference to that in bulk site ($E_{\text{VaH},i}^{\text{Bulk}}$). Supplementary Fig. 8a shows the distribution of hydrostatic stress of the edge dislocation and Supplementary Fig. 8b shows the distribution of $\Delta E_{\text{VaH},i}$ around the dislocation core. Supplementary Fig. 9 shows the shear stress-strain curves at different concentrations of hydrogen-vacancy complexes. It can be seen that the more hydrogen-vacancy complexes are implanted, the stronger pinning effect will be. The critical shear stress (τ_c) for driving dislocation motion also shows a linear response with the line density of hydrogen-vacancy complex (N_{VaH}/L), but with a much steeper slop (101.9 MPa·nm) than that pinned by hydrogen. Our current simulations show that the hydrogen-vacancy complex take an even stronger pinning role than the hydrogen atmosphere.

Supplementary References

1. Wolverton C, Ozoliņš V, Asta M. Hydrogen in aluminum: First-principles calculations of structure and thermodynamics. *Phys. Rev. B* **69**, 144109 (2004).

2. Schaefer HE, Gugelmeier R, Schmolz M, Seeger A. Positron lifetime spectroscopy and trapping at vacancies in aluminium. *Mater. Sci. Forum* **15-18**, 111-116 (1987).

3. Balluffi R. Vacancy defect mobilities and binding energies obtained from annealing studies. *J. Nucl. Mater.* **69**, 240-263 (1978).

4. Wolverton C, Ozoli?? V, Asta M. Hydrogen in aluminum: First-principles calculations of structure and thermodynamics. *Phys. Rev. B* **69**, 1124-1133 (2004).

5. Lu G, Kaxiras E. Hydrogen embrittlement of aluminum: The crucial role of vacancies. *Phys. Rev. Lett.* **94**, 155501 (2005).

254 6.   Apostol F, Mishin Y. Angular-dependent interatomic potential for the aluminum-hydrogen
255   system. *Phys. Rev. B* **82**, 144115 (2010).

256 7.   Mishin Y, Farkas D, Mehl MJ, Papaconstantopoulos DA. Interatomic potentials for
257   monoatomic metals from experimental data and ab initio calculations. *Phys. Rev. B* **59**,
258   3393-3407 (1999).

259 8.   Song J, Curtin WA. Mechanisms of hydrogen-enhanced localized plasticity: An atomistic study
260   using α-Fe as a model system. *Acta Mater.* **68**, 61-69 (2014).

261 9.   Hoover WG. Canonical dynamics: equilibrium phase-space distributions. *Phys. Rev. A* **31**, 1695
262   (1985).

263 10.   Nosé S. A unified formulation of the constant temperature molecular dynamics methods. *J.*
264   *Chem. Phys.* **81**, 511-519 (1984).

265 11.   Plimpton S. Fast parallel algorithms for short-range molecular dynamics. *J. Comput. Phys.* **117**,
266   1-19 (1995).

267 12.   Li J. AtomEye: an efficient atomistic configuration viewer. *Modell. Simul. Mater. Sci. Eng.* **11**,
268   173 (2003).

269 13.   Wilcox B, Smith G. The Portevin-Le Chatelier effect in hydrogen charged nickel. *Acta Metall.*
270   **12**, 371-376 (1964).

271 14.   Boniszewski T, Smith G. The influence of hydrogen on the plastic deformation ductility, and
272   fracture of nickel in tension. *Acta Metall.* **11**, 165-178 (1963).

273